Electronic Supporting Information

Uniaxial-oriented $FA_xMA_{1-x}PbI_3$ films with low intragrain and structural defects for self-powered photodetectors

Li Zhang,[a] Teng Zhang,[a] Yaping Gao,[a] Deliang Cui,[a] Qilong Wang,[b] Gang Lian,[a] Haohai Yu,*[a] huaijin Zhang[a], and Ching-Ping Wong[c]*

[a] State Key Lab of Crystal Materials, Shandong University, Jinan 250100, P.R. China

[b] Key Laboratory for Special Functional Aggregated Materials of Education Ministry, School of Chemistry & Chemical Engineering, Shandong University, Jinan 250100, P.R. China

[c] School of Materials Science and Engineering, Georgia Institute of Technology, Atlanta, Georgia 30332, United States

* Corresponding Authors:

E-mail: liangang@sdu.edu.cn, haohaiyu@sdu.edu.cn

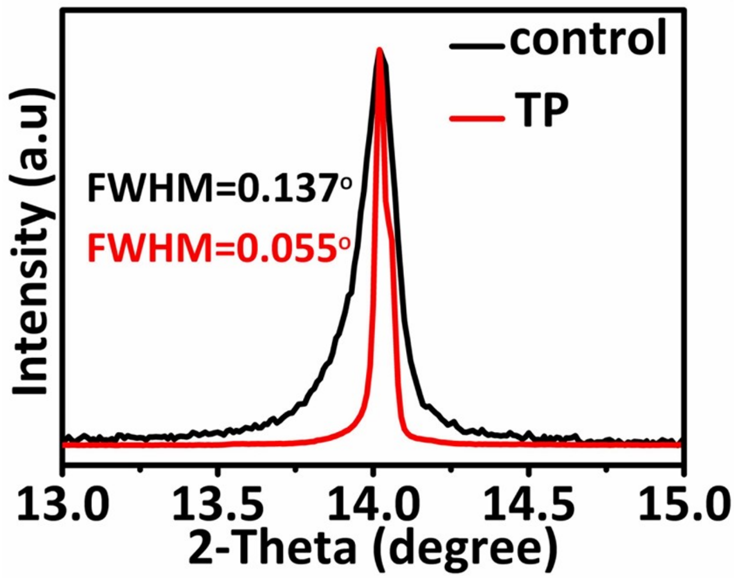

Fig. S1 XRD patterns from 13° to 15° of control and TP films.

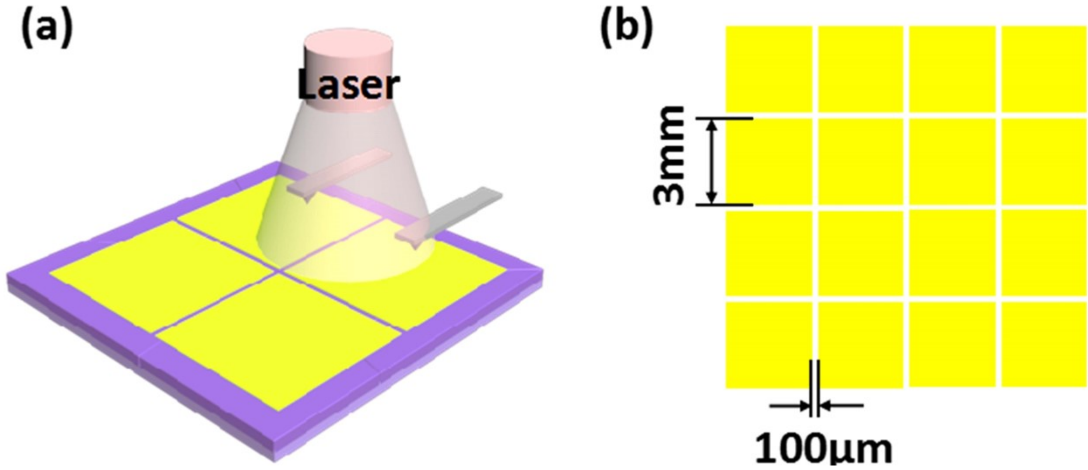

Fig. S2 (a) Schematic of device structure and (b) Mask pattern.

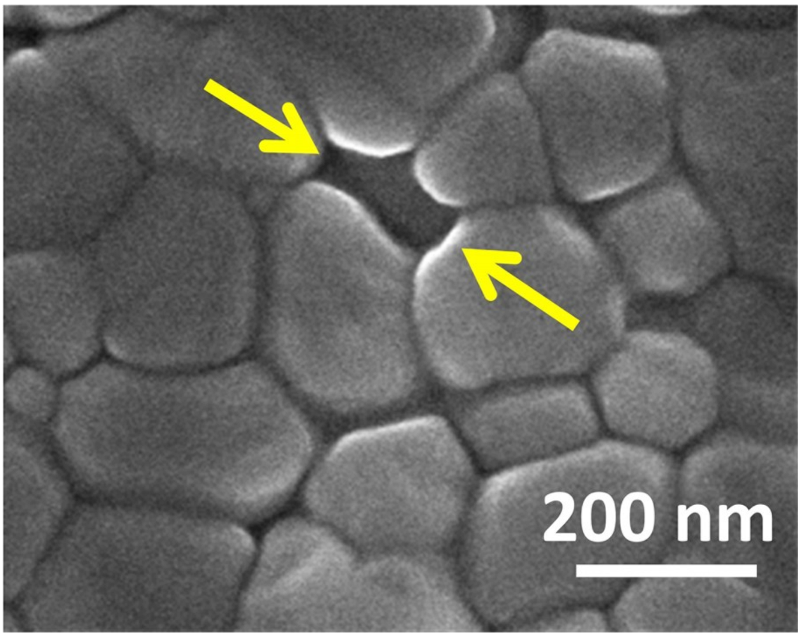

Fig. S3 High-magnification top-view SEM image of SnO_2-control film.

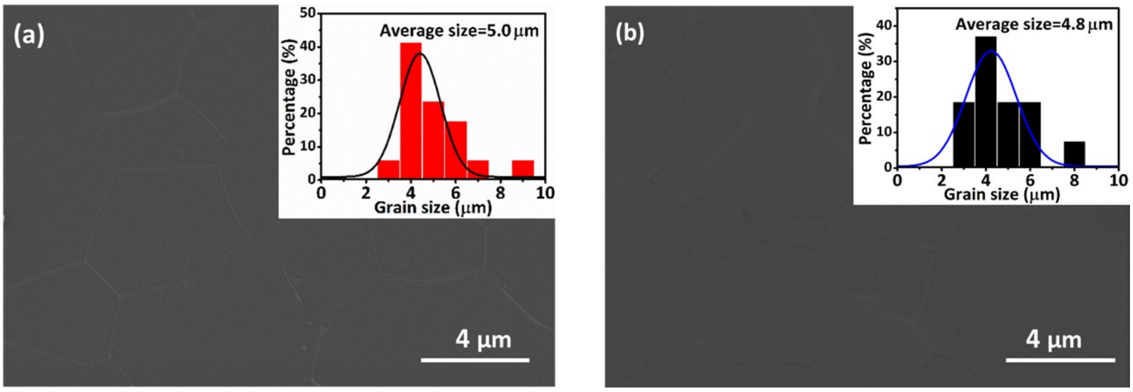

Fig. S4 Top-view SEM images and particle size distribution of (a) SnO_2-TP75 and (b) SnO_2-TP100 films.

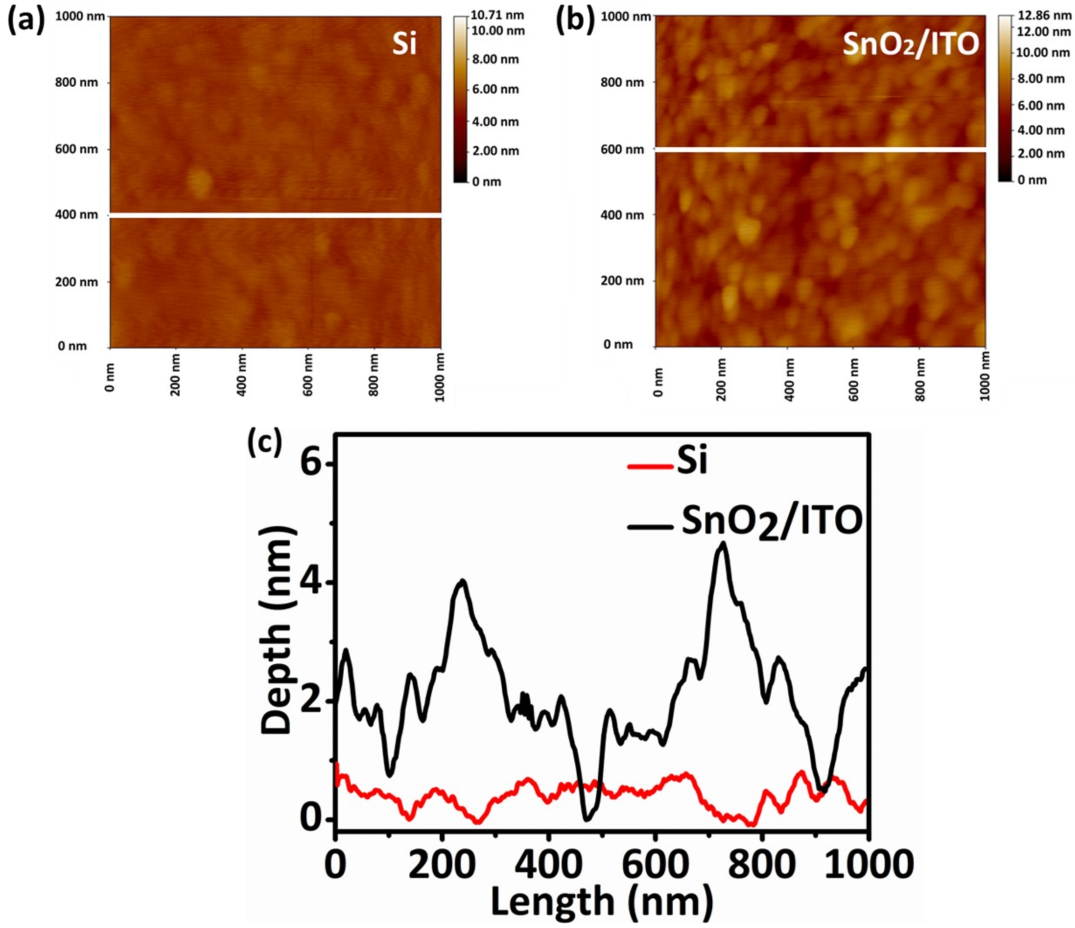

Fig. S5 AFM topographic images of (a) Si substrate and (b) SnO_2/ITO substrate; (c) surface roughness of Si and SnO_2/ITO substrates.

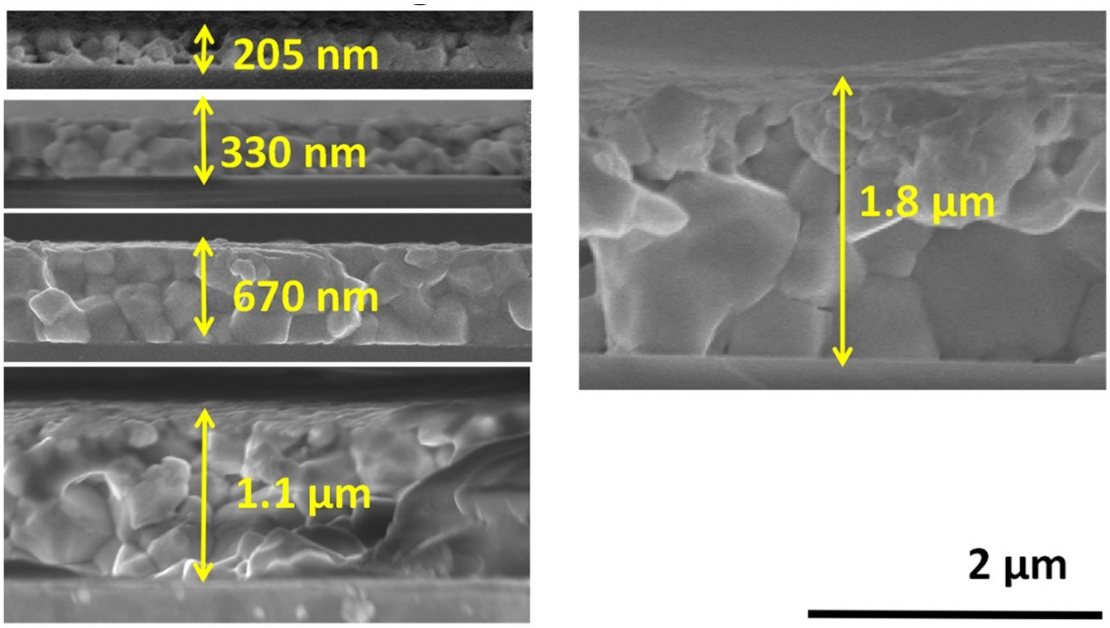

Fig. S6 Cross-section SEM images of SnO_2-control films with different thickness.

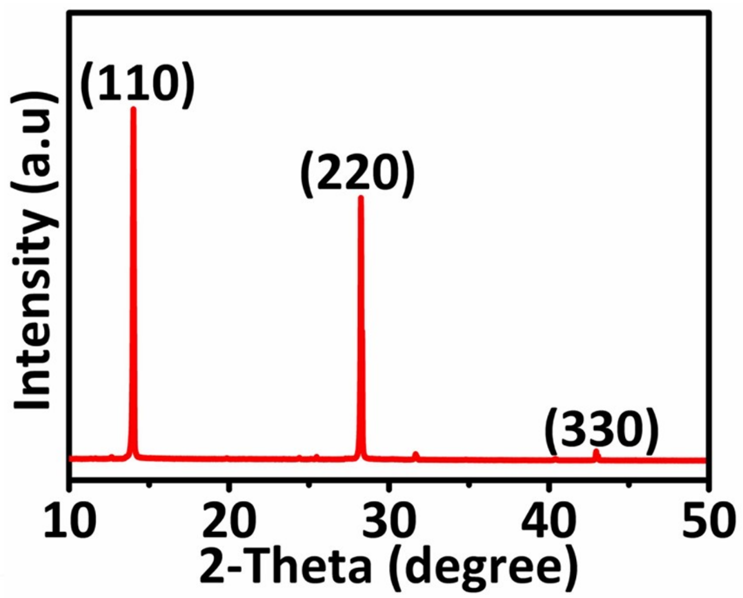

Fig. S7 XRD pattern of SnO_2-TP75 film.

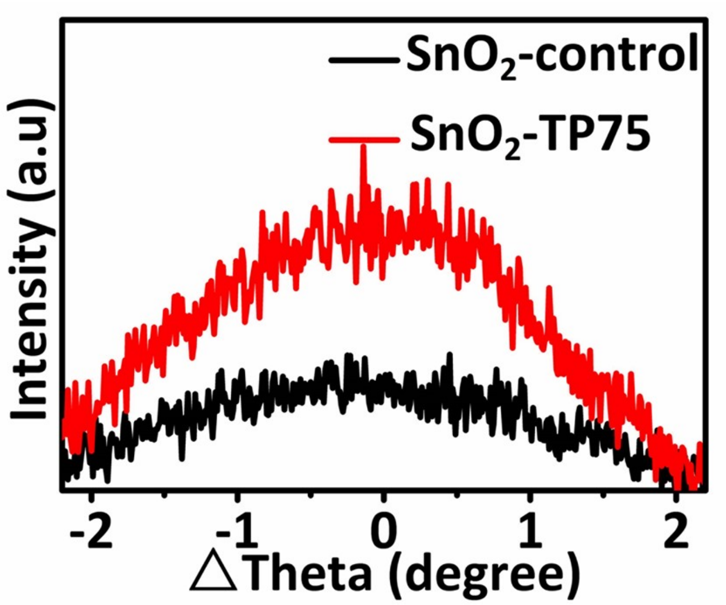

Fig. S8 Rocking curves of SnO_2-control and SnO_2-TP75 films.

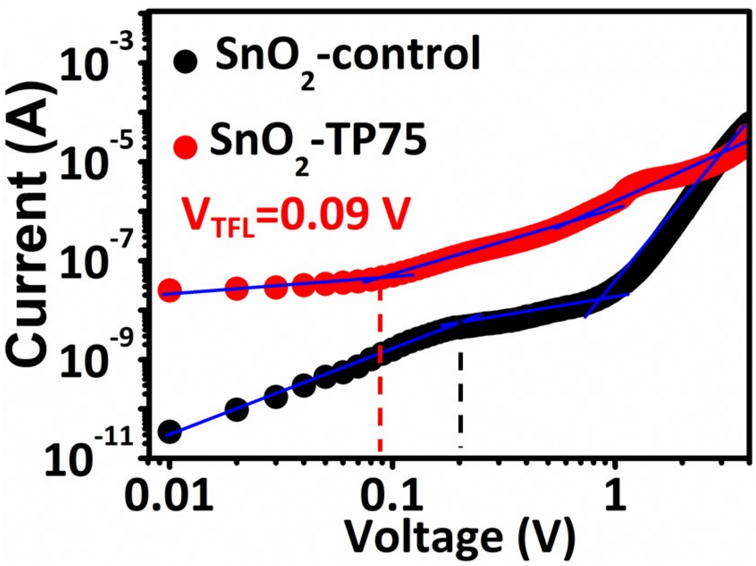

Fig. S9 Dark I–V curve of electron-only photodetector based of SnO_2-control and SnO_2-TP75 films.

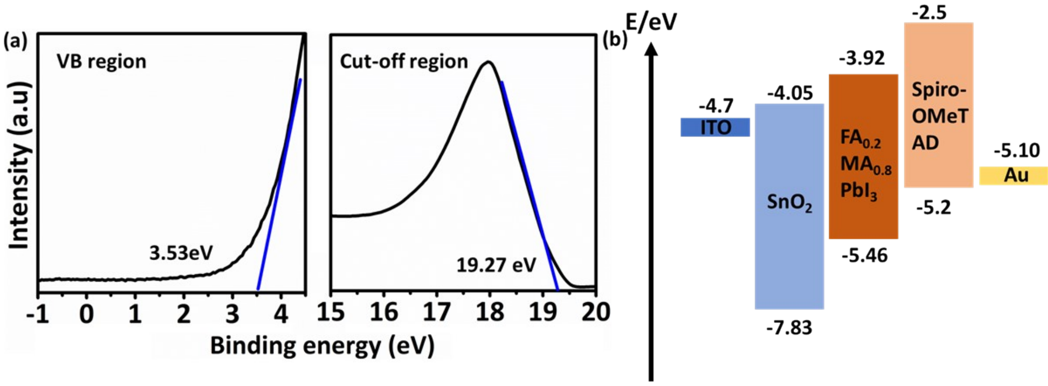

Fig. S10 (a) Ultraviolet photoelectron spectra of SnO_2-TP75 film, (b) diagram of the energy levels of the SPPDs based on SnO_2-TP75 film.

To obtain the diagram of the energy levels of SPPDs, we carried out UPS measurements to profile the CBM and VBM of the SnO_2-TP75 film. Equations (1) and (2) were used for the calculation of Fermi energy (E_f) and E_{VBM}, respectively:

$$E_f = -(hv - E_{cut-off}) \tag{1}$$

$$E_{VBM} = -\left[hv - \left(E_{cut-off} - E_{oneset}\right)\right] = -IE \tag{2}$$

wherein, $E_{cut\text{-}off}$ and E_{onset} are the cut-off and onset energy of the photo-electron signals, respectively, *hv* (21.2 eV) is the photon energy of the He Iα source; *IE* is ionization energy [*Advanced Energy Materials, 2021, 11(28): 2101080*]. According to the above equations, the VBM of SnO_2-TP75 film locates at −5.46 eV. The optical bandgap ($E_{g,opt}$) of SnO_2-TP75 film is extracted from the corresponding absorption spectrum (*Fig. S11*). The $E_{g,opts}$ of SnO_2-TP75 film is 1.54 eV. Thus, the CBM of the SnO_2-TP75 film locates at −3.92 eV. The corresponding diagram of the energy levels associated with the device was shown in *Fig. S10b*.

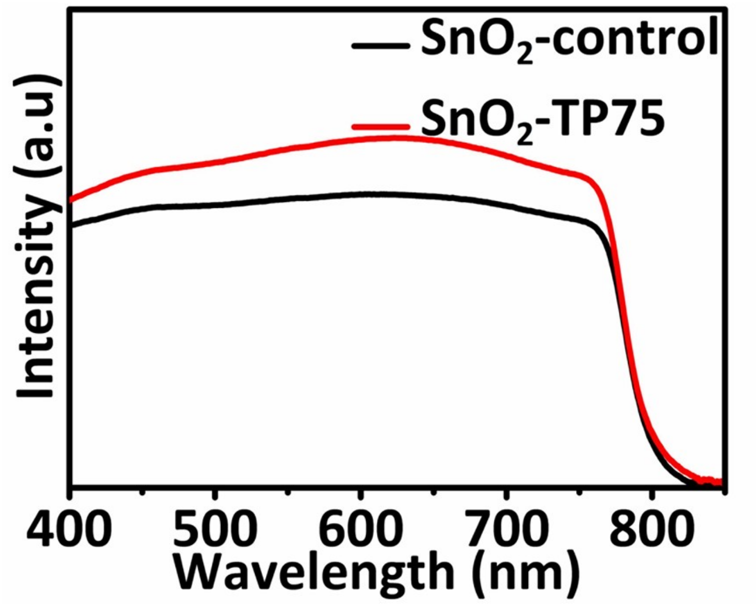

Fig. S11 UV-vis absorptions of SnO_2-control and SnO_2-TP75 film.

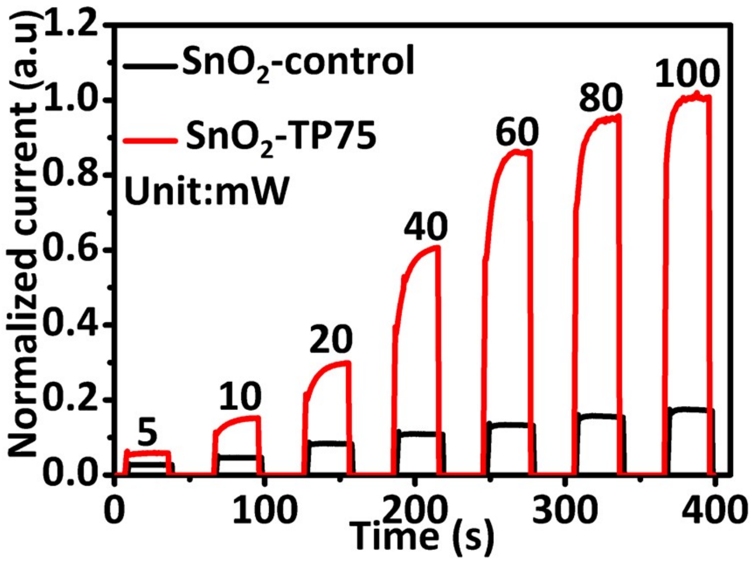

Fig. S12 I−T curves of SPPD based on SnO_2-control and SnO_2-TP75 films under different power intensities of 671 nm laser illumination at a bias of 0 V.

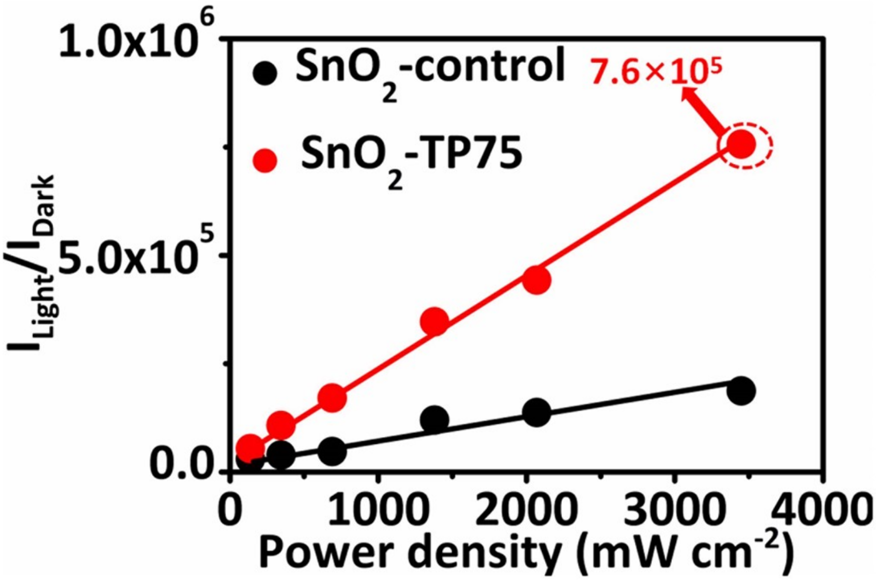

Fig. S13 I_{light}/I_{dark} ratio of SPPD based on SnO_2-control and SnO_2-TP75 films under difffferent power intensities of 671 nm laser illumination at a bias of 0 V.

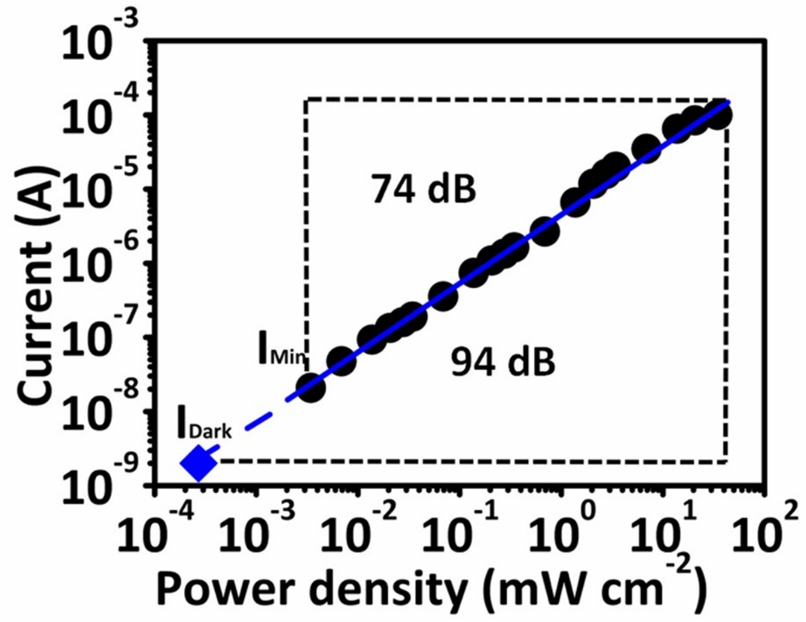

Fig. S14 Linear dynamic range of SPPD based on SnO_2-TP75 film under 671 nm laser illumination at a bias of 0 V.

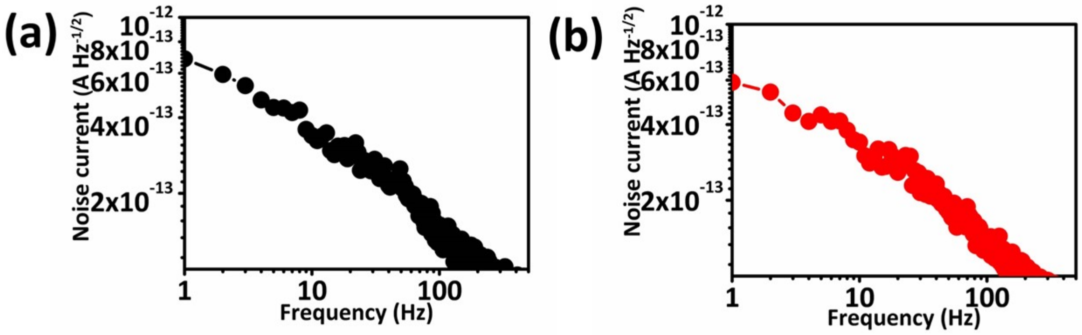

Fig. S15 Frequency-dependent noise current of SPPD based on perovskite films at a bias of 0 V (a) SnO_2-control film and (b) SnO_2-TP75 film.

Detectivity (D^*) is used to evaluate the performance of photodetector. It can be calculated via the equation $D^* = \frac{R\sqrt{AB}}{i_n}$, where *A* is the active area of the device, *B* is the detection bandwidth and i_n is the noise current. In this work, i_n is generally dominated by *1/f* noise in the low-frequency region. As shown in *Fig. S15*, when the frequency is 50 Hz, the detected *1/f* noise currents of the two devices are 0.22 pA $Hz^{-1/2}$ and 0.21 pA $Hz^{-1/2}$. On increasing the frequency over 50 Hz, the noise of devices gradually approach the shot noise limit ($i_{shot} = (2eI_dB)^{1/2}$) of 0.18 pA $Hz^{-1/2}$ and 0.2 pA $Hz^{-1/2}$. With continuously increasing the frequency, D^* can be calculated from the shot noise. However, according to $D^* = \frac{R\sqrt{AB}}{i_n}$, the lower i_n, the larger D^* value. Therefore, the modulation frequency was set to 50 Hz.

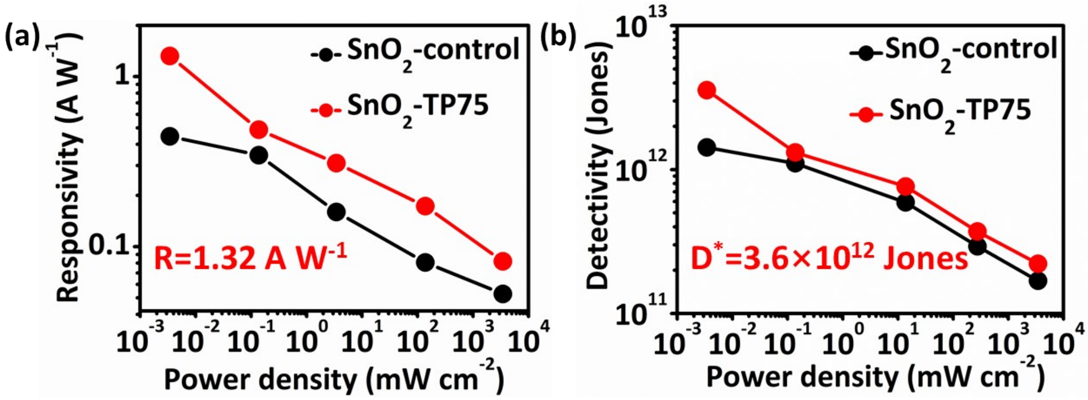

Fig. S16 (a) Responsivity and (b) detectivity of photodetectors based on SnO_2-control and SnO_2-TP75 films under 671 nm laser illumination at a bias of 1 V.

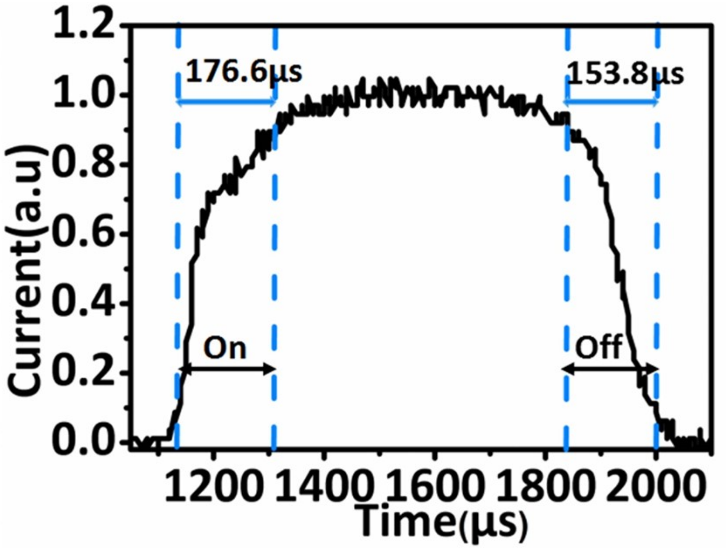

Fig. S17 Response-recovery time curve of SPPD based on SnO_2-control film under 671 nm laser illumination at a bias of 0 V.

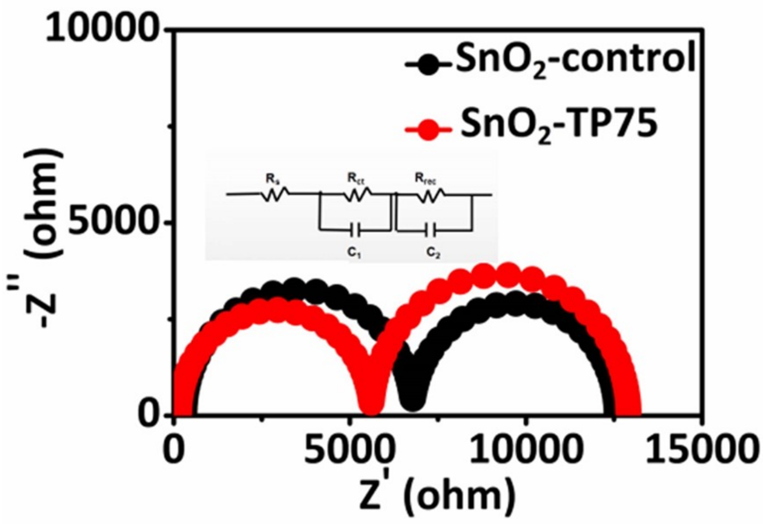

Fig. S18 Nyquist plots of photodetector based on SnO_2-control and SnO_2-TP75 films.

Table S1. The bi-exponential equation parameters for fitting the TRPL curves of control and TP films.

Sample	τ_1	A_1	τ_2	A_2	τ_{ave}
Control film	19.3 ns	72.3%	239.6 ns	27.7%	201.4 ns
TP film	120.2 ns	37.9%	985.8 ns	62.1%	925.8 ns

Table S2. The bi-exponential equation parameters for fitting the TRPL curves of SnO_2-control and SnO_2-TP75 films.

Sample	τ_1	A_1	τ_2	A_2	τ_{ave}
SnO_2-Control film	21.0 ns	85.7%	265.7 ns	14.3%	187.0 ns
SnO_2-TP75 film	66.2 ns	45.5%	630.9 ns	54.5%	585.4 ns

Table S3. Key figure-of-merit values for SPPD fabricated in the present study compared with those of devices reported in the literature.

Structure	Responsivity (mA W^{-1})	Detectivity (Jones)	Wavelength (nm)	Ref.
$Si/SnO_2/MAPbI_3/MoO_3$	50.9	2.23×10^{12}	300-1150	1
ITO/PEDOT:PSS/$MAPbI_3$/PCBM/Ag	436	3.125×10^{10}	300-800	2
ITO/Triazine-Th-OMeTAD/$MAPbI_3$/$PC_{61}BM$/BCP/Ag	470	8.2×10^{12}	300-780	3
Ag/spiro-OMeTAD/$MAPbI_3$/ZnO:PBI-H/ITO	350	2.5×10^{13}	370-770	4
FTO/c-TiO_2/$Cs_{0.05}MA_{0.16}FA_{0.79}Pb(I_{0.9}Br_{0.1})_3$/Spiro-OMeTAD/Au	520	8.8×10^{12}	300-810	5
ITO/SnO_2/$MAPbI_3$/ Carbon	260	7.01×10^{11}	400-800	5
FTO/NiO_x/$MAPbI_3$/PCBM/$PPDIN_6$/Ag	63.7	1.27×10^{12}	300-800	6
ITO/P3HT/Perovskite/Spiro-OMeTAD/Ag	410	6.1×10^{10}	410-780	7
SVO/$Cs_{0.05}(FA_{0.85}MA_{0.15})_{0.95}Pb(I_{0.85}Br_{0.15})_3$/Ag	42.5		400-750	8
ITO/PTAA/$FAPbI_3$/C_{60}/BCP/Ag	450	1.18×10^{12}	350-800	9
ITO/SnO_2/$Cs_xDMA_{1-x}PbI_3$ films/PCBM/Bphen/Cu	380	1×10^{13}	420-700	10
GZO NRs/$MAPbI_3$/MoO_3/Au	340	1.6×10^{12}	350-800	11
ITO/SnO_2/$FA_{0.2}A_{0.8}Pb_{I3}$/Spiro-OMeTAD/Au	**470**	**3.4×10^{12}**	**340-800**	**This work**

Table S4. Key figure-of-merit values for SPPD fabricated in the present study compared with those of devices reported in the literature under the specific wavelengths

Structure	Responsivity (mA W^{-1})	Detectivity (Jones)	Test conditions	Ref.
$Au/CH_3NH_3PbI_3$/MWs/Ag	160	1.3×10^{12}	520nm/9×10^{-3} mw cm^{-2}	12
FTO/CdS_{10}/$MAPbI_3$/Spiro-OMeTAD/Ag	480	2.1×10^{13}	700nm/4.57×10^{-3} mw cm^{-2}	13
Al/$CH_3NH_3PbI_3$nanowires/Ni	227	1.36×10^{11}	532nm/1×10^{-5} mw cm^{-2}	14
ITO/CdS/$MAPbI_3$/Au	430	2.3×10^{11}	730nm/10 mw cm^{-2}	15
ITO/SnO_2/$Cs_{0.05}(FA_{0.85}MA_{0.15})_{0.95}Pb(I_{0.85}Br_{0.15})_3$/Spiro-OMeTAD/Ag	473	1.35×10^{13}	720nm/ 5.4×10^{-3} mW cm^{-2}	16
ITO/PMMA/$MAPbBr_3$/Au	380	1.7×10^{12}	520nm/10×10^{-3} mw cm^{-2}	17
ITO/PTAA/$Cs_xFA_{1-x}Pb(I_{1-y}Br_y$/PCBM/BCP/Cu	403	6.1×10^{13}	650nm/73×10^{-3} mw cm^{-2}	18
ITO/PEDOT:PSS/$MAPb(I_{1-x}Br_x)_3$/PCBM/Ag	31	4×10^{9}	780nm/6.36 mw cm^{-2}	19
ITO/PEDOT:PSS/$MAPbI_3$/PMMA/PCBM/Ag	460	3.18×10^{10}	671nm/6.5 mw cm^{-2}	20
ITO/ZnO:PBI-H/$MAPbI_3$/Spiro-OMeTAD/Ag	350	2.5×10^{13}	670nm/126×10^{-3} mw cm^{-2}	4
ITO/SnO_2/$FA_{0.2}A_{0.8}Pb_{I3}$/Spiro-OMeTAD/Au	**512**	**3.4×10^{12}**	**671nm/3.4×10^{-3} mw cm^{-2}**	**This work**

References

1 W. Qu, S. Weng, L. Zhang, M. Sun, B. Liu, W. Du and Y. Zhang, *Appl. Phys. Express*,2020, **3**, 121001.

2 Z. Ma, Y. Zhang, T. Li, X. Tang, H. Zhao, J. Li, C. Ma and J. Yao, *Appl. Phys. A Mater. Sci. Process.*, 2020, **126**, 869.

3 C. Shan, F. Meng, J. Yu, Z. Wang, W. Li, D. Fan, R. Chen, H. Ma, G. Li and A. K. K. Kyaw, *J. Mater. Chem. C*, 2021, **9**, 7632–7642.

4 Q. Zhang, M. Shou, Y. Xu, J. Zheng, X. Wen, Y. Zhao, H. Wang, L. Liu and Z. Xie, *J. Mater. Chem. C*, 2020, **8**, 16506–16512.

5 G. R. Adams, V. O. Eze, M. A. S. Shohag, R. Simpson, H. Parker and O. I. Okoli, *Eng. Res. Express*, 2020, **2**, 015043.

6 J. Wang, S. Xiao, W. Qian, K. Zhang, J. Yu, X. Xu, G. Wang, S. Zheng and S. Yang, *Adv. Mater.*, 2021, **33**, 2005557.

7 D. Wang, W. Xu, L. Min, W. Tian and L. Li, *Adv. Mater. Interfaces*, 2022, **9**, 2101766.

8 R. Xu, L. Min, Z. Qi, X. Zhang, J. Jian, Y. Ji, F. Qian, J. Fan, C. Kan, H. Wang, W. Tian, L. Li, W. Li and H. Yang, *ACS Appl. Mater. Interfaces*, 2020, **12**, 16462–16468.

9 X. Feng, M. Tan, M. Li, H. Wei and B. Yang, *Nano Lett.*, 2021, **21**, 1500–1507.

10 L. Li, F. Zhang, S. Ye, X. Peng, Z. Sun, J. Lian, L. Liu, J. Qu and J. Song, *Nano Energy*, 2020, **71**, 104611.

11 H. Zhou, L. Yang, P. Gui, C. R. Grice, Z. Song, H. Wang and G. Fang, *Sol. Energy Mater. Sol. Cells*, 2019, **193**, 246–2521.

12 Y Wu, P Wang, F Ting, B Wang, C Xie, W li, W Wang, Adv. Electron. Mater., 2019, 5(5): 1900135.

13 F. Cao, L. Meng, M. Wang, W. Tian and L. Li, *Adv. Mater.*, 2019, 31(12): 1806725.

14 J. Tao, Z. Xiao, J. Wang, C. Li, X. Sun, F. Li, X. Zou, G. Liao and Z. Zou, *J. Alloys Compd.*, 2020, **845**, 155311.

15 Z. Li, H. Li, K. Jiang, D. Ding, J. Li, C. Ma, S. Jiang, Y. Wang, T. D. Anthopoulos and Y. Shi, *ACS Appl. Mater. Interfaces*, 2019, **11**, 40204–40213.

16 W. Tian, L. Min, F. Cao and L. Li, *Adv. Mater.,* 2020, **32**, 1906974.

17 C. Li, J. Li, C. Li, J. Wang, X. Tong, Z. Zhang, Z. Yin, D. Wu and L. Luo, *Ad. Optical Mater.*,2021, **9**, 2100371.

18 E. López-fraguas, B. Arredondo, C. Vega-colado, M. Naja, D. Martín-martín, Y. Galagan, J. M. Sánchez-pena, R. Vergaz and B. Romero, *Organic Electronics*, 2019, **73**, 292–298.

19 S. Qiao, Y. Liu, J. Liu, G. Fu and S. Wang, *ACS Appl. Mater. Interfaces*, 2021, **13**, 34625-34636.

20 Y. Liu, S. Qiao, H. Sun, J. Liu, L. Guo, Z. Yang, G. Fu and S. Wang, *ACS Appl. Nano Mater.*, 2021, **4**, 1682-1691.